Article

UAV Data Collection Co-Registration: LiDAR and Photogrammetric Surveys for Coastal Monitoring

Carmen Maria Giordano *⬥, Valentina Alena Girelli ⬥, Alessandro Lambertini ⬥, Maria Alessandra Tini ⬥ and Antonio Zanutta ⬥

Department of Civil, Chemical, Environmental and Materials Engineering (DICAM), University of Bologna, Viale Risorgimento 2, 40136 Bologna, Italy; valentina.girelli@unibo.it (V.A.G.); alessandro.lambertini@unibo.it (A.L.); mariaalessandra.tini@unibo.it (M.A.T.); antonio.zanutta@unibo.it (A.Z.)
* Correspondence: carmenmaria.giordano@unibo.it

Abstract: When georeferencing is a key point of coastal monitoring, it is crucial to understand how the type of data and object characteristics can affect the result of the registration procedure, and, above all, how to assess the reconstruction accuracy. For this reason, the goal of this work is to evaluate the performance of the iterative closest point (ICP) method for registering point clouds in coastal environments, using a single-epoch and multi-sensor survey of a coastal area (near the Bevano river mouth, Ravenna, Italy). The combination of multiple drone datasets (LiDAR and photogrammetric clouds) is performed via indirect georeferencing, using different executions of the ICP procedure. The ICP algorithm is affected by the differences in the vegetation reconstruction by the two sensors, which may lead to a rotation of the slave cloud. While the dissimilarities between the two clouds can be minimized, reducing their impact, the lack of object distinctiveness, typical of environmental objects, remains a problem that cannot be overcome. This work addresses the use of the ICP method for registering point clouds representative of coastal environments, with some limitations related to the required presence of stable areas between the clouds and the potential errors associated with featureless surfaces.

Keywords: UAV; photogrammetry; LiDAR; co-registration; monitoring; coastal survey

1. Introduction

Coastal areas are constantly under the pressure of both natural and anthropic activities, which can influence the regular changes in coastal morphology.

The littoral in the municipality of Ravenna (Emilia-Romagna, Italy) is the most vulnerable in the Mediterranean [1–4] due to factors that over the past eighty years have converged synergically in the reduction in the available coastal area, endangering the local activities and subjecting the aquifer to salinization risk: the presence of more frequent extreme weather phenomena, the sea level rising, the transportation reduction in fluvial and alongshore sediment, the alteration of the territory and of the dune system for urban development and recreational facilities, the development of emerged barriers, and the aggravation of the subsidence phenomena due to the extraction of underground fluids (water and gas).

The adoption of informed management decisions is critical for safeguarding these vulnerable areas, supported by the analysis of local coastal trends, thanks to the use of an effective monitoring system [5].

Surveying and monitoring of coastal areas are the current themes of interest in the geomatics field, where very different techniques can be used, i.e., punctual measurement can be

performed by means of GNSS (Global Navigation Satellite System) receivers [6–8] and total stations and levels, requiring contact with the object; instead, a non-contact survey of a wide range of points is possible by means of remote sensing techniques, exploiting both active and passive sensors, mounted on non-contact systems such as video systems [9,10], satellites [11–14], manned aircrafts [11,15,16], and Unmanned Aerial Vehicles (UAVs) [6–8,17–20].

The technique selection is linked to factors that can shape the survey planning process [21] and set some preferences in the kind of system and sensor to be used, as follows:

- Context: the area in which the object is can set some physical constraints (e.g., flight height limit, inaccessible areas, obstacles, etc.).
- Object: shape, extent, and surface characteristics.
- Survey goal: output type, quality, and final use.
- Time, operators, and instrument availability.
- Elaboration: given that it is generally not a unique pipeline, specific elaboration requirements need to be considered during the data acquisition process.

A limited amount of 3D points can be acquired by means of a GNSS receiver [7] (e.g., transects or point networks), but when a higher spatial resolution is required, there is a need of using a less time-consuming method that allows the acquisition of a dense dataset, such as cameras [10,13,17] (optical, thermal, multispectral, hyperspectral), SAR (Synthetic Aperture Radar) [14], and LiDAR (Light Detection and Ranging) [16]. Large areas are preferably acquired by satellite or airborne data, while small and middle areas can also be captured by UAV or video data. However, satellite data have a temporal constraint related to orbit time, and for a higher or flexible temporal resolution, it is preferable to use an airplane, UAV, or video system.

UAV systems have become widely used for environmental survey and monitoring of small and middle extent [19], thanks to the low cost of small drones combined with the increasing accessibility of data elaboration. However, the greatest advantage of using a UAV system for coastal monitoring is its flexibility on the scale [20] and the morphology of the object and on the survey goal: in other words, it is crucial in the ability of shaping the flight planning to the survey needs and collecting high-resolution data in a short time (the most extensive time is used for the flight planning and for the data elaboration, but the actual survey is strictly limited by the system itself). The UAV is a remote sensing system that can be also exploited in inaccessible areas and for rapid subsequent post-storm assessment [8]. However, a direct georeferencing of an inaccessible area, with its advantages and limitations, is possible if the UAV system is integrated with a GNSS receiver capable of acquiring phase observables, allowing a positioning correction method [22,23] such as Real-Time Kinematic (RTK), Network Real-Time Kinematic (NRTK), or Post-Processed Kinematic (PPK). Otherwise, there is the mandatory need of ground measurements in order to optimize the reconstruction [24,25]. Moreover, the UAV system is composed of integrated or interchangeable sensors, allowing the acquisition of different descriptions of the same scene. In practice, data integration is not commonly implemented due to the increase in the time required for both the survey and the processing phase when utilizing multiple sensors and systems. However, data integration [26] is a method to assess the reconstruction accuracy and to improve the description of object complexity. For example, LiDAR and photogrammetry allow both to produce a tridimensional reconstruction of the scene, but the result is strictly connected to how the object responds to the sensor and how the elaboration can affect the result.

The LiDAR sensor is an active sensor able to directly acquire the range data, which can be then optimized by the information collected by the Inertial Navigation System (INS) and the GNSS receivers. The LiDAR point cloud has no inherent redundancy, and the quality of the point cloud is mostly related to the instrument used and the calibration of its sensors.

The multi-echo technique, typical of the LiDAR system, allows the collection of hidden ground data by the vegetation, a better reconstruction of the Digital Terrain Model (DTM). However, the LiDAR data, by itself, do not provide a semantic description of the area and need to be integrated with an optical camera.

The bidimensional acquisitions conducted by an optical camera necessitate processing to obtain a tridimensional representation of the area through a photogrammetric elaboration. Currently, it constitutes a relatively fast computation attributable to the advent, over the past two decades, of algorithms that have significantly streamlined the elaboration procedures, such as the Structure-from-Motion technique [27,28]. The advantage of this technique is that it also allows the reconstruction of the scene for unstructured and uncalibrated data: in fact, the mere knowledge of the location of the tie points in the image reference system allows the solution of the Bundle Block Adjustment (BBA) in an arbitrary reference system. Then, the introduction in the compensation of heterogeneous measures, such as the GNSS data of some Ground Control Points (GCPs) or of the shooting locations, can retrieve the external parameters in an absolute reference system. However, the photogrammetric elaboration has two main problems: it cannot reconstruct the ground data hidden by the vegetation, because their points are not visible in the images; it is sensitive to areas where it can be difficult to find reliable tie points, such as homogeneous textured areas or instable areas (moving elements or reflective surfaces).

Therefore, the use of different techniques allows to acquire different types of data and a different perspective of the same scene, reaching a higher description of the area complexity [29] and a higher control on the data accuracy. Data fusion approach or continuous monitoring work emphasizes the importance of data co-registration, which requires their mutual alignment to a standardized reference system to facilitate integration or comparison.

In the literature [30,31], numerous techniques are available for performing point cloud registration: the direct georeferencing allows the exploitation of the GNSS data of the flight for the model registration in the desired geographic datum, with a subsequent data projection in the chosen cartographic and altimetry system; the indirect georeferencing is based on the computation of the transformation parameters from the local reference system to the absolute one, exploiting conjugate elements or the point cloud geometry. In particular, the indirect registration is possible thanks to the use of different procedures:

- Target-based method: The collimation of homologous points on different outputs, such as targets, allows the definition of a transformation function between the slave point cloud and the reference one. Moreover, the knowledge of the target coordinates (GCPs) in a specific datum allows the cloud georeferencing in the coordinate system of the used GCPs.
- Feature-based method: Feature extraction from the point clouds, similarity measurement for finding conjugate features, and finally computation of the registration parameters (e.g., using geometric primitives such as planes, spheres, cylinders, and tori [32] or using linear features [33]). The feature-based method does not require an overlap between the two point clouds, but only the possibility of extracting the same type of features and the visibility of the same features in multiple clouds.
- Iterative closest point (ICP) method (between points or surfaces): there are different variants of the algorithm [34,35], and the basic idea is to find the transformation parameters that minimize the distance between the slave point cloud or data shape and the master one. This type of algorithm needs the presence of an overlapping area, and often, a coarse pre-alignment of the two clouds in order to enhance the final minimization computation is suggested.

- Probabilistic methods: the point clouds are visualized as probability distributions, and the registration is conducted by minimizing the two data distributions, exploiting, for example, the Gaussian mixture model (GMM) for clustering the point data [36].

The co-registration process is a many-sided topic that is usually addressed on the basis of the following four main drivers:

- Type of data that need to be registered (images, point clouds, DEM, etc.).
- Type of final reference system (relative or absolute).
- Type of survey (single-epoch or multi-epoch).
- Type of sensor (single-sensor or multi-sensor).

For example, ref. [37] evaluates the co-registration of multispectral and RGB orthomosaics obtained by the photogrammetric processing of UAV image data, changing the type of transformation, the number of GCPs, and their distribution; ref. [38] proposes an automatic procedure for the co-registration of multi-epoch block-images acquired by the UAV system using key points detectable in the stable part of the survey area, bypassing the requirement for GCPs if no absolute registration is needed; ref. [39] proposes a method for the co-registration of LiDAR point clouds acquired by terrestrial and UAV system, exploiting correspondences between canopy shapes projected on the ground planes; ref. [40] describes a method for the co-registration of multi-sensor point clouds, identifying matching key points on their related height maps; ref. [41] focuses on the enhancement of the registration of photogrammetric outputs in an absolute reference system combining the use of GCPs and the PPK correction method of the UAV location, thus evaluating the impact of the number and the distribution of GCPs; ref. [42] investigates the use of NRTK, PPK, and PPP correction methods of the UAV position, in order to perform the registration of photogrammetric outputs in an absolute reference system bypassing the need to establish GCPs; ref. [43] evaluates the use of LiDAR and imagery UAV for coastal monitoring, with a co-registration of the data exploiting a PPK correction method of the UAV location or the use of GCPs.

In this wide collection of specific problems, the goal of this work is to evaluate the ICP registration process performed between two different point clouds describing the same coastal area, and both need to be registered in an absolute reference system for monitoring purposes.

These two point clouds represent the same epoch of a multi-sensor survey and processing: the first point cloud is generated by a photogrammetric processing of an image dataset collected by an optical camera onboard a UAV, and the second one is collected by a LiDAR system onboard a UAV. For the main purpose of the work, the coordinates of some targets collected on the study area by a GNSS receiver are exploited.

To perform the ICP process, an overlapping area between the two point clouds is needed, i.e., a single-epoch survey simplifies the process, because the collected area is unchanged; however, the use of different sensors can lead to dissimilarities between the two clouds. For these reasons, the main objective is to evaluate and identify potential errors related to co-registration through the ICP algorithm in a coastal environment for the final enhancement of the co-registration process tied to the minimization of the error causes.

2. Materials and Methods

The entire workflow can be schematized as shown in (Figure 1), outlining the main phases of the work: from defining the study object, through planning and survey, and finally to the processing and co-registration stages. For each phase, three main systems are used for the coastal survey: a UAV system equipped with an optical camera; a UAV system equipped with a LiDAR sensor; and a GNSS receiver as a rover with an NRTK acquisition correction mode. Each system has its own processing workflow (vertically), but some outputs can be used to integrate or validate data at specific stages of the process.
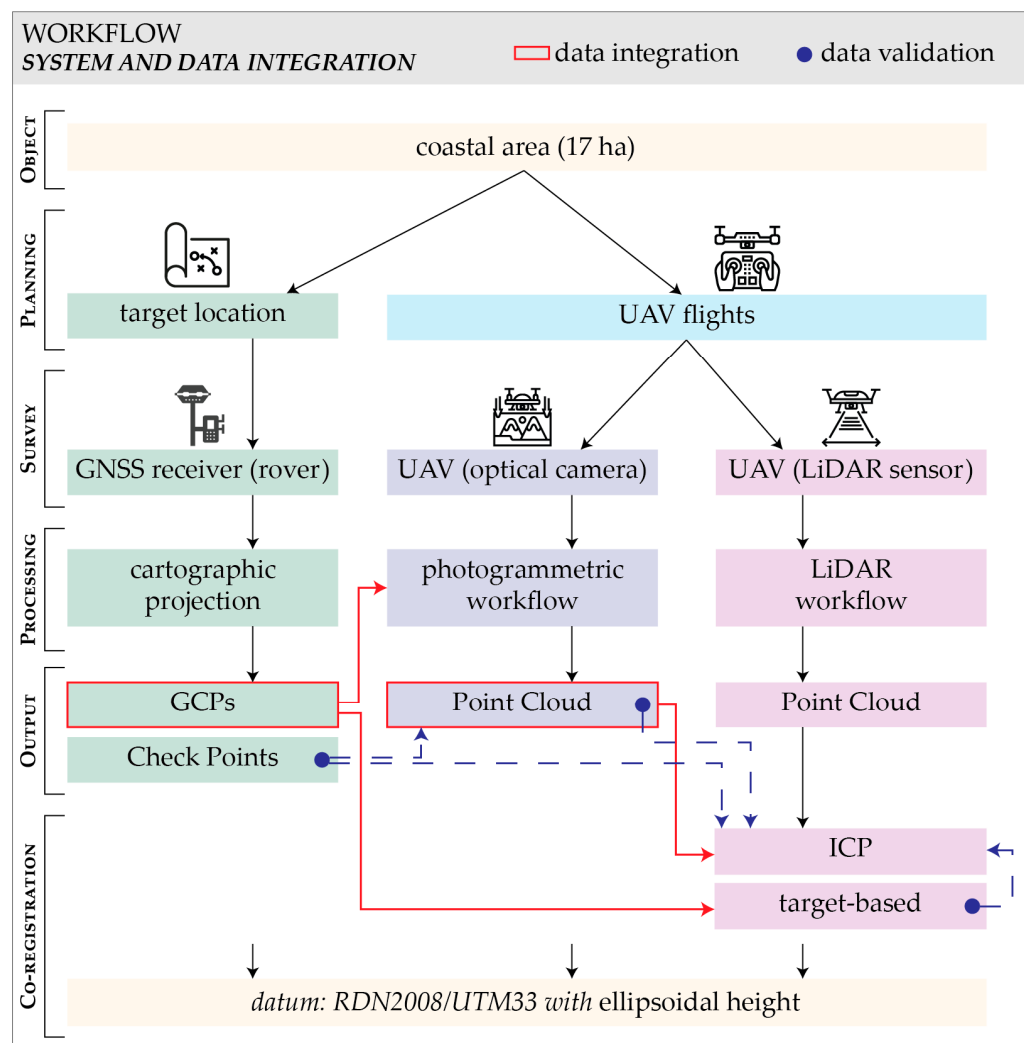
Figure 1. The workflow of the entire process: object, planning, survey, processing, output, and co-registration. The red rectangle identifies data that have been integrated into a specific chain of the process, while the blue circle identifies data that have been used for validation purposes.

2.1. Study Site

The surveyed area (ca. 17 ha) is located on the Northern Adriatic coast between the villages of "Lido di Classe" and "Lido di Dante" (Ravenna, Emilia-Romagna, Italy).

The area proposed in this paper represents a subset of a larger study area (Figure 2) monitored by the Geomatics group of the Department of Civil, Chemical, Environmental, and Materials Engineering (DICAM) of the University of Bologna for the LIFE NatuReef project [44]. This European project has the goal of restoring biogenic reefs, thanks to the work of native ecosystem engineers, oysters (*Ostrea edulis*) and sabellariid worms (*Sabellaria spinulosa*), who are able to create three-dimensional structures, in order to retain sediments, dissipate wave energy, counteract the erosional coastal trend, and, at the same time, enhance the local marine biodiversity.

The monitored area, near the Bevano river mouth, is a nature reserve, a rare slice of territory still not urbanized and not subjected to intense tourist development. This area is characterized by wood, dune, and beach systems, as well as by the presence of fresh, brackish, and marine waterbodies. This territory is threatened by coastal erosion, flooding, and saline intrusion, which are emphasized by the sea level rise, the lack of natural nourishment of the beaches, the increasing frequency and intensity of storm surges, and the subsidence phenomena.
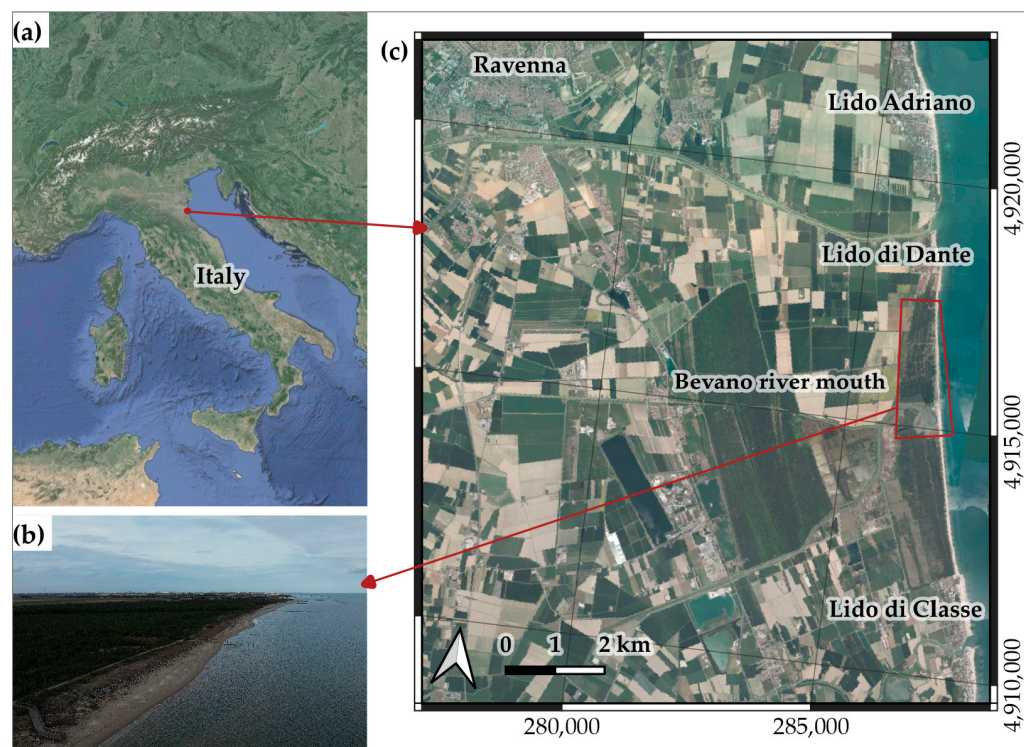
Figure 2. (**a**) Study site's general location. Background: google satellite map; (**b**) aerial oblique capture of the area from P1 payload onboard the UAV "DJI Matrice 300 RTK", taken on 2023-11-09; (**c**) study site near Ravenna (Emilia-Romagna, Italy). Background: Orthophoto AGEA 2020 (r_emiro:2022-03-10T115056), map coordinate reference system RDN2008/UTM33 (EPSG 6708), and meter unit.

2.2. GNSS Data Survey and Processing

The GNSS receiver TopCon Hiper V was used to acquire the absolute location of a set of ground points (Figure 3). The position correction mode was based on a Network Real-Time Kinematic (NRTK) service [45], exploiting the creation of a Virtual Reference Station (VRS) [46] near the surveyed area.

This method allows the real-time acquisition of data framed in the national datum ETRS89-RDN2008 [47,48], based on dual-frequency observations acquired by the rover, whose ambiguities can be estimated through the computation of the double differences with the observations acquired by a permanent network of reference stations, allowing a measurement collection with a demonstrated accuracy of a few centimeters [49–51].

The strategic planning of targets is essential for enhancing the efficiency of the survey in terms of both required time and correct distribution. The distribution of the targets needs to follow two main goals: they have to be located in positions not obstructed by the vegetation, in order to be visible in all the images; they have to cover homogeneously and redundantly the whole survey area, in order to minimize the possible artifacts during the photogrammetric elaboration (such as the bowl effect [25]) and also in order to use some of them as check points (CPs), which are points used only for the evaluation of the reconstruction accuracy.

The constraints placed by the territory morphology can be overcome by exploiting different targets (Figure 4) that are related both to the scene availability and the distribution planning: when the space is sufficient and not covered by the vegetation, a circular plywood target is used (a diameter of 50 cm, with a black and white pattern); otherwise, a square plastic target (10 × 10 cm, with a black and white pattern) is placed on top of the available wood elements; moreover, some pins are used to establish a local permanent network for monitoring purposes.
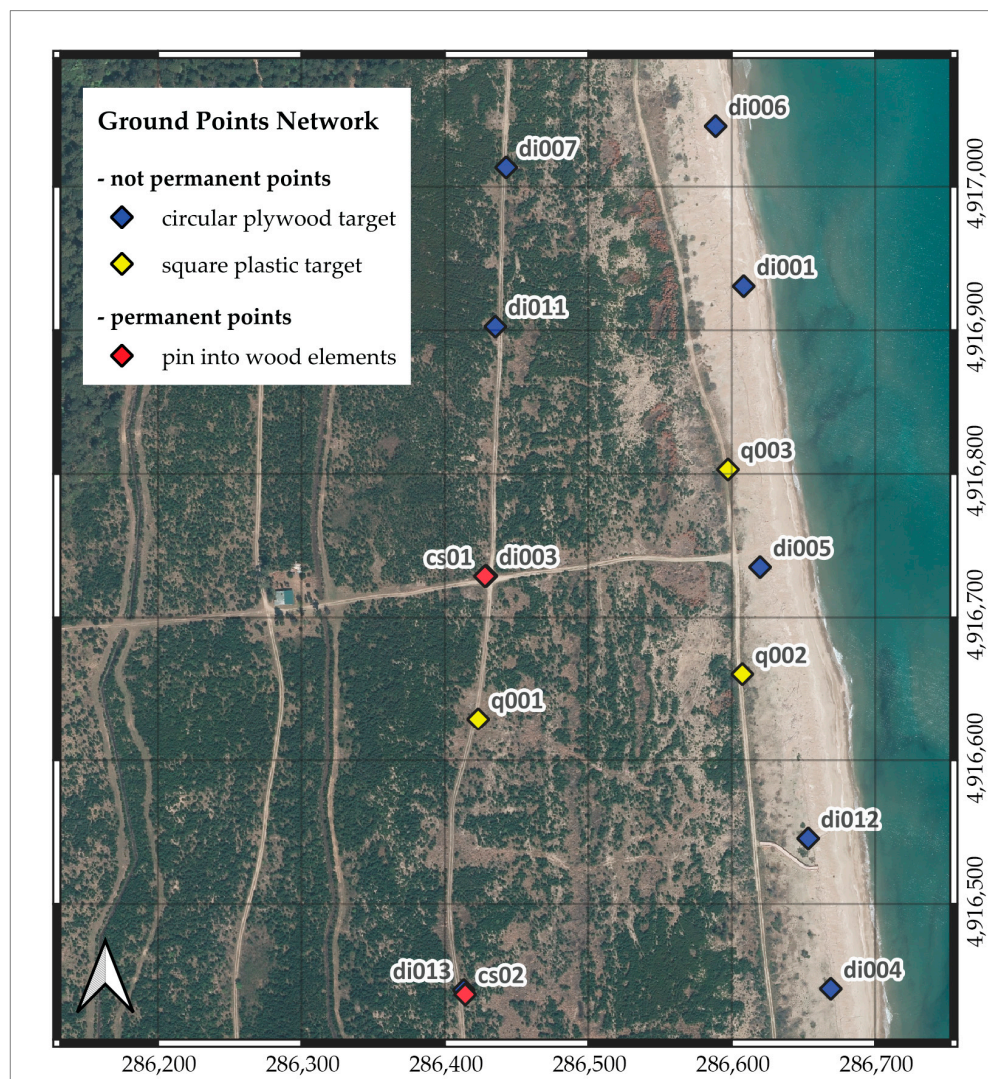
Figure 3. The network of the ground points collected on the area and surveyed by means of the GNSS receiver TopCon Hiper V in the NRTK mode. Background: Orthophoto AGEA 2020 (r_emiro:2022-03-10T115056), map coordinate reference system RDN2008/UTM33 (EPSG 6708), and meter unit.

The whole network of 14 points was collected in about 2 h, due to the necessary distances traveled by the surveyor between the remote points. Targets were left in their surveyed location for the entire duration of the UAV flights, to support the processing of UAV data. In the absence of signal-related problems, the position acquisition of a single point takes about 3 min: 2 min for the target placement; 1 min for the observation acquisition and ambiguity fixing. A position measurement is statistically computed from the 60 acquisition epochs and has a linked precision assessment: their evaluation shows the average and maximum horizontal standard deviation (SD) of 1.3 cm and 1.4 cm, respectively, and the estimated average and maximum vertical standard deviation of 2.1 cm and 3.6 cm, respectively.

The processing of the GNSS data of the ground points is performed by the software ConvER2021 [52], available on the Emilia-Romagna web portal. In particular, the target coordinates, framed in the geographic system ETRS89-RDN2008 with the ellipsoidal height, are transformed into the projected cartographic system RDN2008/UTM33 with the orthometric height, using the IGM (*Istituto Geografico Militare*) gridded data gk-2, based on the geoid model ITALGEO2005 [53]. However, the further elaboration of the UAV data is conducted by exploiting their projected cartographic coordinates while maintaining the

ellipsoidal height. This choice is related to the compatibility problem that can occur dealing with the data integration, emphasized by the fact that often the software used does not allow an automatic management of the height conversion through the Italian geoid. This underscores the necessity of estimating the mean geoid height of the area, which can be later applied into the final model as a vertical shift. For each ground point, the difference in its ellipsoidal and orthometric heights is computed, showing a mean geoid height of 39.039 m with a standard deviation of 3 mm.
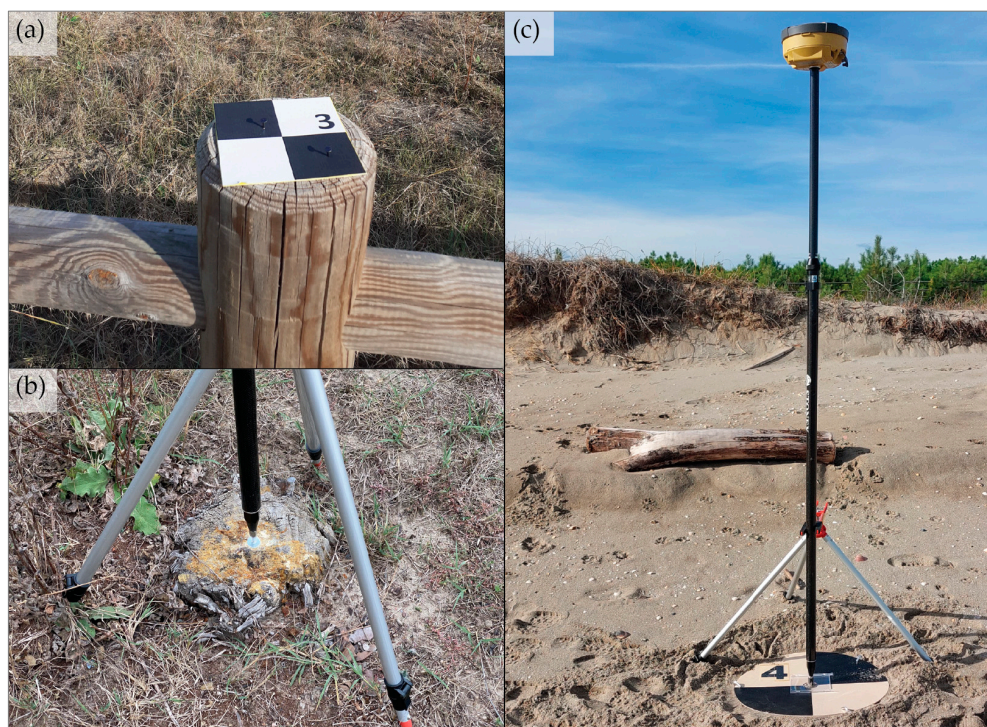

Figure 4. The use of different targets related to scene availability: (**a**) the square plastic target, 10 × 10 cm with a black and white pattern; (**b**) a pin into the wood element; and (**c**) the circular plywood target, diameter of 50 cm, with a black and white pattern.

2.3. UAV Flights

Two UAV flights were performed over the area, exploiting the low tide of the day (9 November 2023), by the DJI Matrice 300 RTK (Figure 5a) [23], with dimensions of 810 × 670 × 430 mm (without rotors), and the maximum take-off weight of 9 kg, with a maximum payload of 2.7 kg, equipped with the DJI P1 payload (optical camera) and later the DJI L1 (LiDAR sensor). The DJI D-RTK 2 Mobile Station (Figure 5b) was installed on the area to obtain a real-time correction of the UAV position, offering an accuracy of 1 cm + 1 ppm horizontally and 1.5 cm + 1 ppm vertically. The relative positioning between the master station and the rover is computed. However, as a result of the recording of the master coordinates by a single-point positioning mode, absolute positioning is inapplicable.

The UAV photogrammetric survey was carried out by a planned flight (Table 1) with the DJI Pilot 2 software. The flight started at 1:18 pm and ended at 1:43 pm (GMT), capturing 1253 pictures at the fixed flight height of about 45 m, due to flight constraints in the nature reserve, setting a forward and side overlap of 80% and 50%, respectively.
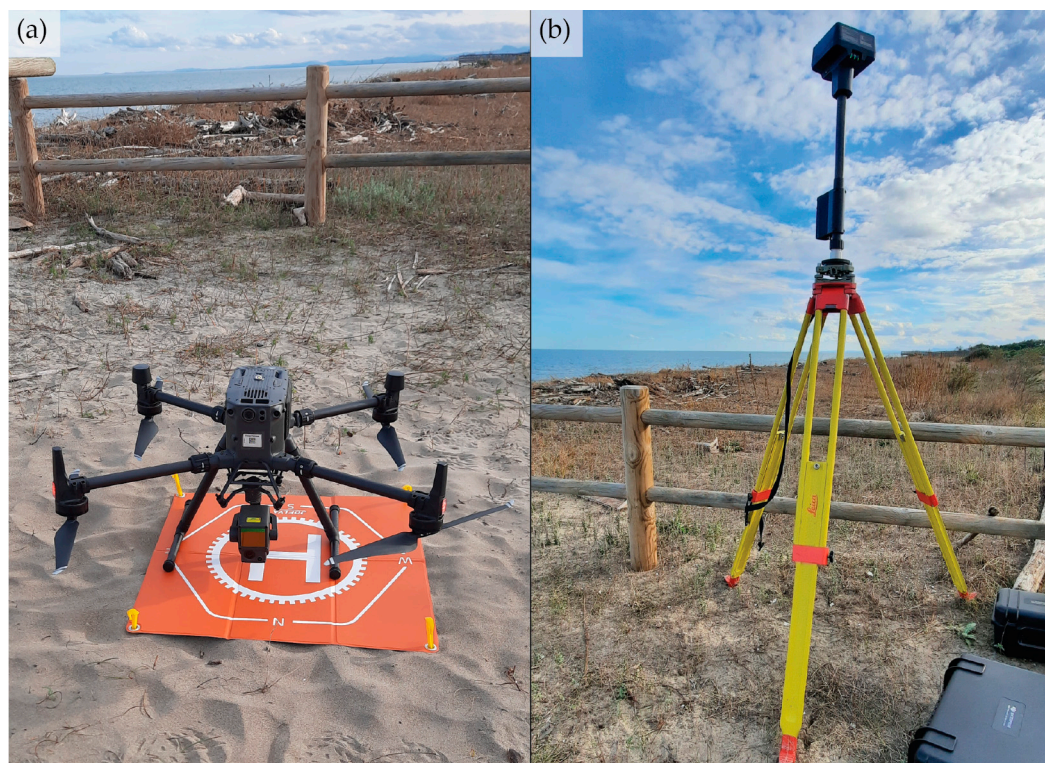
Figure 5. (**a**) DJI Matrice 300 RTK with L1 payload onboard; (**b**) D-RTK 2 Mobile Station.

Table 1. The parameters of the UAV photogrammetric flight and the visual representation of the image capture locations during the flight. Background: Orthophoto AGEA 2020 (r_emiro:2022-03-10T115056), map coordinate reference system RDN2008/UTM33 (EPSG 6708).

Flight Parameters		
payload	DJI Zenmuse P1	
sensor type	optical camera	
sensor dimension	36 × 24 mm	
image resolution	8192 × 5460 pixel	
focal length (f)	35.00 mm	
pixel length (l_{pix})	4.39 μm	
forward overlap	80%	
side overlap	50%	
flight height (D) from take-off point	45 m	
mean photo scale ($1:S_p$) $S_p = D/f$	1:1300	
GSD = $l_{pix} \cdot D/f$	0.57 cm	
flight speed	5.4 m/s	
surveyed area	~17 ha	
number of images	1253	
acquisition time	~25 min	

The EXIF (exchangeable image file format) metadata embedded within the images contain all the acquisition parameters recorded during the flight, such as the image capture

locations in the WGS84 reference system and the corresponding attitude: the values of yaw, pitch, and roll are recorded both for the vehicle and the gimbal. Furthermore, the integration of a gimbal onboard the UAV contributes to compensating for the frame movement, allowing a consistent nadiral capture during the flight.

The collected pictures have an excellent Ground Sample Distance (GSD) of about 6 mm (Table 1). However, coastal areas have two main identifiable problems that can compromise the photogrammetric reconstruction:

- Moving elements, such as vegetated areas and water bodies, are not stable elements, and thus, they could be an issue during the orientation phases and the dense correlation.
- Homogeneous textured areas, such as sand areas, are not distinctive, and they may provide weaker tie points.

The UAV LiDAR survey was conducted by a planned flight (Table 2) with the DJI Pilot 2 software. The flight started at 2:00 p.m. and ended at 2:20 p.m. (GMT), capturing the site by a repetitive scanning mode from the fixed height of about 45 m, setting a side strip overlap of 20%. The collection of 454 images, with a forward and side overlap of 70% and 37%, respectively, grants the point cloud coloring. According to the manufacturer's specifications, within a distance of 50 m, this system grants a vertical accuracy of 5 cm and a horizontal accuracy of 10 cm.

Table 2. The parameters of the UAV LiDAR flight and the visual representation of the shooting locations during the flight. Background: Orthophoto AGEA 2020 (r_emiro:2022-03-10T115056), scale 1:10,000, map coordinate reference system RDN2008/UTM33 (EPSG 6708) (*cam.* for "camera"; *LiDAR* for "Light Detection and Ranging").

Flight Parameters	
payload	DJI Zenmuse L1
sensor type	LiDAR with an integrated optical camera
camera model	EP800
sensor dimension (cam.)	1 inch
focal length (cam.)	8.8 mm
picture resolution (cam.)	5472 × 3648 pixel
side overlap (LiDAR)	20%
forward overlap (cam.)	70%
side overlap (cam.)	37%
flight height (from take-off point)	45 m
cloud density	395 point/m^2
GSD (cam.)	1.23 cm
flight speed	5.3 m/s
return mode (LiDAR)	triple
scanning mode (LiDAR)	repetitive
surveyed area	~17 ha
number of images	454
estimated time	~20 min
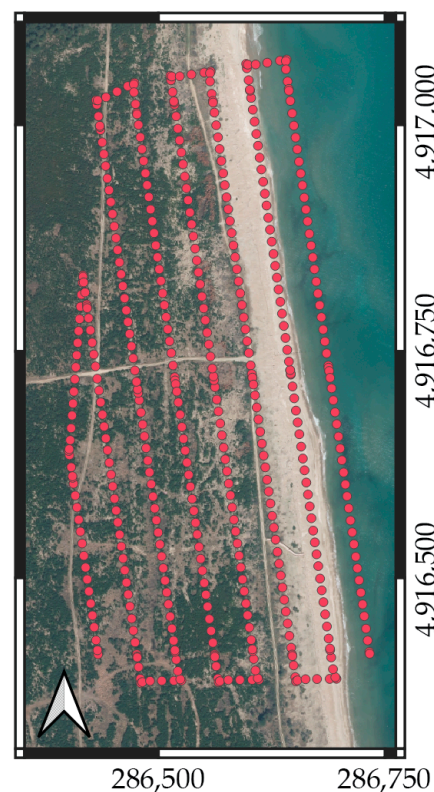
2.4. Photogrammetric Workflow

The photogrammetric workflow is not a unique pipeline, but it can be shaped by the data availability, the software used, and the user's experience and sensitivity in identifying and resolving specific problems.

The software exploited for the photogrammetric elaboration is MicMac [54–58], a free and open-source software developed around 2005 at the *Institut national de l'information géographique et forestière* (IGN) and the *École nationale des sciences géographiques* (ENSG).

This software implements the SfM technique and allows a great level of customization, and in this work context, it is exploited using its simplified tools accessible by the command line.

The photogrammetric workflow (Figure 6) is composed as follows (a detailed description of the scripts concerning this elaboration is accessible in the Supplementary Materials):
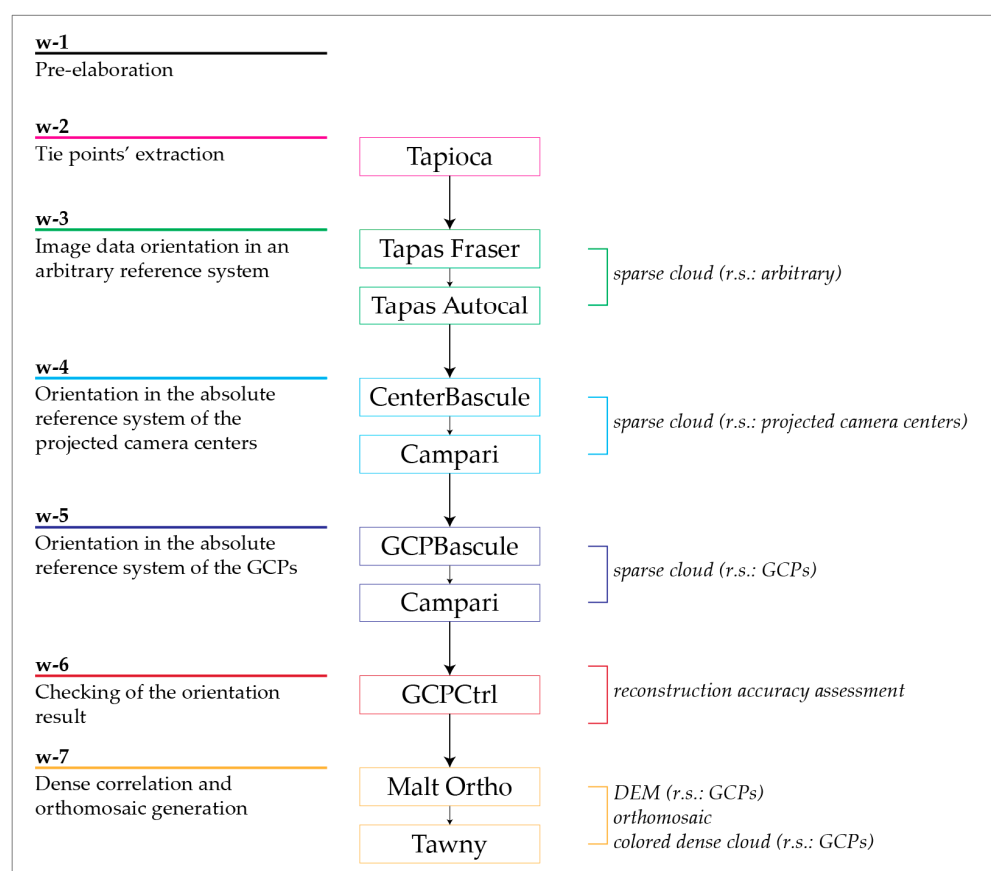

Figure 6. The MicMac pipeline for the photogrammetric reconstruction of the image data collected by the UAV system (r.s. for the reference system).

(w-1) Pre-elaboration

A preliminary phase is conducted to adjust the dataset to the specific requirements of the elaboration process: the removal of unsuitable images (pictures with only water features); retrieval of the image locations by the Exif Tool software [59]; conversion of the data to the XML format; projection of the geographic coordinates into a Euclidean system based on a local tangent plane with the origin in the center of the images; computation of the image pairs thanks to the knowledge of their locations; and computation of an image sub-pattern for the camera pre-calibration.

(w-2) Tie points' extraction

The tie points' detection is facilitated due to the use of an XML file containing the image pairs to be used for the procedure, based on the knowledge of the shooting locations.

(w-3) Image data orientation in an arbitrary reference system

Firstly, a camera pre-calibration is performed with a small group of images. The calibration model chosen is the Fraser one and is composed of 12 parameters: focal length, (x,y) coordinates of the PPA (Principal Point of Autocollimation), (x,y) coordinates of the PPS (Principal Point of Symmetry), n.3 symmetric radial distortion, n.2 decentering distortion parameters, and n.2 affine distortion parameters (residual = 0.62 pixel).

Then, the images are oriented in an arbitrary reference system, computing the internal and external orientation parameters for the whole dataset, exploiting the calibration parameters calculated previously as the initial value of the BBA (residual = 0.68 pixel).

(w-4) Orientation in the absolute reference system of the projected camera centers

The refinement of the orientation parameters is performed by the introduction of the projected camera centers in the BBA (setting an accuracy of the GNSS data of about 0.05 cm).

The transformation highlights a wrong location recorded for some pictures in a middle strip, characterized by a large residual. To mitigate the negative influence of the absolute data for these pictures, the related XML files are removed from the directory of the shooting centers. This allows the orientation refinement combining the GNSS data of the camera centers and the homologous points, linking the images by only the location of the tie points where the GNSS data are not present (residual = 0.59 pixel).

(w-5) Orientation in the absolute reference system of the GCPs

The absolute orientation in the reference system of the GCPs (di001, di003, di004, di005, di006, di007, di011, di012, di013) is performed using their projected coordinates in the cartographic system RDN2008/UTM33, while maintaining the ellipsoidal height. All the orientation parameters are refined, setting a GCP acquisition accuracy of about 0.03 m and a collimation accuracy of about 0.5 pix (residual = 0.59 pixel; RMS = 0.013 m with the maximum value of 0.022 m).

(w-6) Checking of the orientation result

Some points of the ground network are used as check points (cs01, cs02, q001, q002, q003) to evaluate the reconstruction accuracy (RMS = 0.053 m; max = 0.101 m).

(w-7) Dense correlation and orthomosaic generation

The dense correlation is processed, exploiting a coarse-to-fine strategy, and ending the procedure at ¼ the original resolution of the images. The problem of the vegetation reconstruction [60] can be solved by setting the correlation window to 3 × 3 pixel and the correlation coefficient to 0.

The orthomosaic is computed, merging the ortophotos and performing a radiometric equalization, in order to obtain a homogeneous output (see the Supplementary Materials, Figure S2).

2.5. Lidar Workflow

The acquired LiDAR data are processed through the software DJI Terra Pro [61], a closed-source software that allows a limited user interaction.

The main settings for the processing are the following:

- The transformation of the coordinate reference system: from WGS84 to WGS84/UTM33 with the ellipsoidal height.
- The optimization of the data acquired (INS and GNSS data).
- The generation of a height density cloud (maximum resolution).
- No smoothing process of the cloud roughness, in order to preserve the scene discontinuity.
- Point ground classification: gentle slope, iteration angle of 6°, and iteration distance of 0.5 m.
- DTM creation at the resolution of 0.1 m.

2.6. Co-Registration

The co-registration procedure (Figure 7) of the two clouds (photogrammetric and LiDAR) is needed to perform any type of integration or comparison. The photogrammetric cloud, as a result of the processing conducted, is already framed in the specified coordinate reference system (RDN2008/UTM33). Conversely, the LiDAR point cloud requires precise registration.
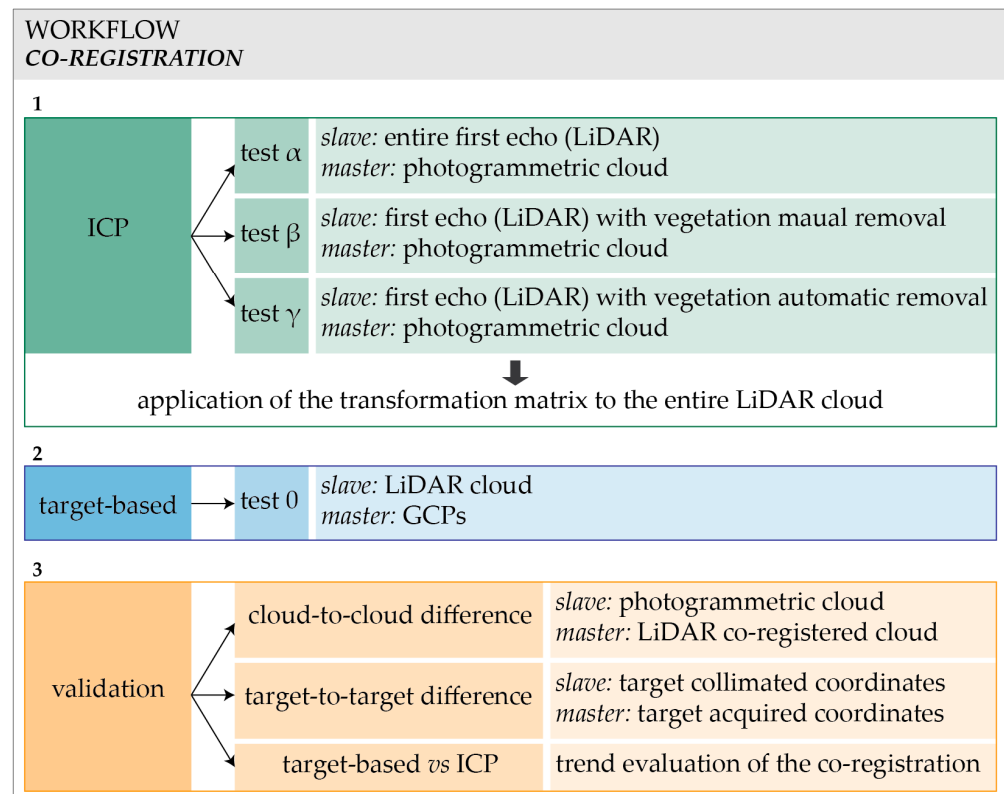

Figure 7. The workflow of the co-registration stage. Step 1: the ICP procedure (test α, test β, test γ); step 2: the target-based procedure (test 0); step 3: the final validation of the ICP procedure (in the Section 3).

The registration of the LiDAR cloud in the same reference system as the photogrammetric one is performed by exploiting two alternatives (ICP and target-based procedure), using the open-source software CloudCompare [62].

2.6.1. ICP Procedure

Before running the ICP algorithm, a preliminary alignment of the point clouds is conducted using 5 GCPs collimated in both point clouds (di006, di005, di004, di013, di007). Subsequently, different ICP assessments are performed, changing the points taken into account in the computation.

The ICP algorithm is based on the reduction in the differences between the two clouds, and the only requirement is the presence of an overlapping area. In this case, the two clouds represent the same object in the same temporal range. However, the LiDAR and photogrammetric clouds show some differences: the LiDAR cloud has a lower spatial resolution (approx. 3 cm for the LiDAR one and approx. 1 cm for the photogrammetric one), and the photogrammetric cloud has a worse reconstruction of the vegetation; the LiDAR technique allows the acquisition of multiple return echoes, a partial collection of ground points hidden by the vegetation, while the photogrammetric elaboration allows the

reconstruction of only the seen scene. These discrepancies may lead to a problem regarding the success of the ICP procedure.

Consequently, we performed different tests, evaluating the impact of the point subset exploited for the alignment. In particular, we implemented 3 tests (Figure 7): test α uses as slave cloud the entire first echo, the return echo that best approximates the photogrammetric cloud; test β uses a portion of the first echo, segmented with a manual and coarse removal of the vegetation (Figure 8a); and test γ uses a portion of the first echo with an automatic removal of the vegetation (Figure 8b). The underlying idea of these tests is to execute an ICP procedure that reduces the influence of the main problematic points, which reflect the dissimilarity in the reconstruction performed by the two sensors.
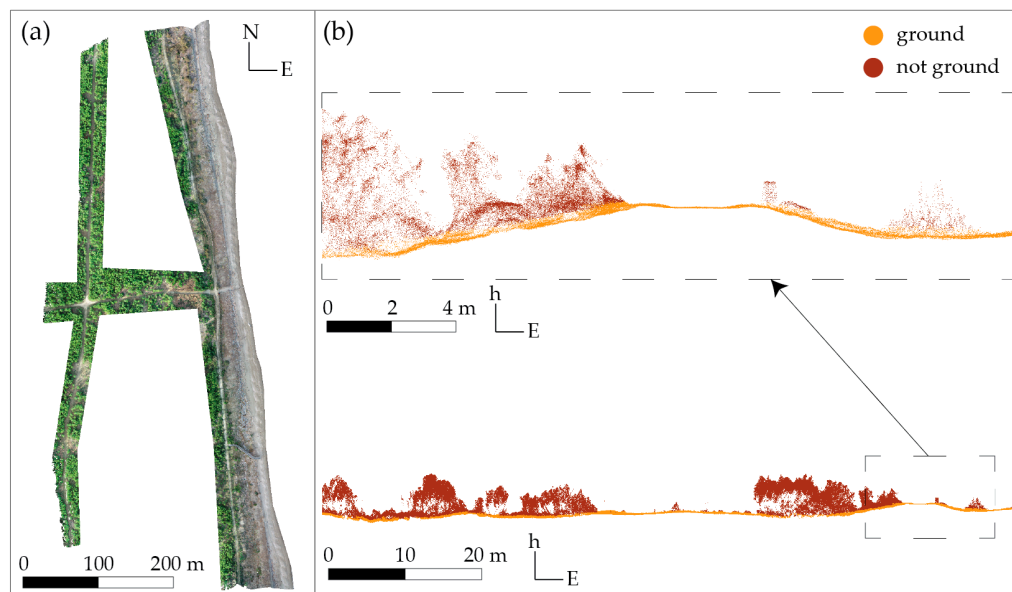

Figure 8. Vegetation removal: (**a**) manual coarse vegetation removal for test β; (**b**) automatic ground/not ground classification for test γ.

After the ICP procedure, the related transformation matrix can be applied to the entire first echo or to the entire LiDAR cloud, ending the co-registration process.

2.6.2. Target-Based Procedure

The collimation of certain GCPs (di003, di005, di012, di004, di001, di006, di007, di013, di011) within the LiDAR cloud and their precise coordinates acquired by the GNSS receiver enables the computation of a transformation matrix in order to roto-translate the cloud in the reference system of these GCPs.

It is important to emphasize that the collimation accuracy in the LiDAR cloud is quite poor, so this procedure is mainly performed to obtain a registered product for validating purposes, defined as test 0. In fact, the peculiarity of this target-based procedure is that it is not performed between the two clouds, but between the LiDAR cloud (slave) and the network of ground points (master), thereby making the co-registration result independent from the photogrammetric elaboration.

3. Results

The LiDAR and photogrammetric data are processed separately, obtaining two point clouds describing the same area, but with different characteristics. While the photogrammetric cloud is already framed in the reference system RDN2008/UTM33, the LiDAR cloud must be registered in the same reference system, and the registration assessment is

conducted through three analyses (Figure 7): the evaluation of the cloud-to-cloud difference (photogrammetric and transformed LiDAR); the assessment of the target-to-target difference (acquired by the GNSS receiver and collimated on the LiDAR cloud); and the trend evaluation between the ICP and target-based registration.

3.1. Cloud-to-Cloud Difference

A global computation of the differences between the two clouds along the height component is performed, using the transformed LiDAR first echo as the reference data and the photogrammetric cloud as the compared data, because the LiDAR cloud has a major area coverage and a more stable point frequency in the vegetated areas. The photogrammetric cloud is subsampled at a minimum spatial resolution of 5 cm, with the objective of reducing the overall cloud weight and decreasing the computation time, obtaining a cloud resolution consistent with that acquired through the LiDAR survey.

The cloud-to-cloud difference has an associated error of about 7 cm (σ_Δ), along the height component, and this parameter is exploited for defining three ranges:

- Negligibility range ($-\sigma_\Delta \leq x \leq \sigma_\Delta$), in which the difference values are not significant in relation to the associated error.
- Acceptability range ($-2\sigma_\Delta \leq x \leq 2\sigma_\Delta$), in which the difference values are significant in relation to the associated error, while defining acceptable values of the co-registration process.
- Inaccuracy range ($x < -2\sigma_\Delta$ or $x > 2\sigma_\Delta$), in which the difference values are significant to define an improper co-registration process.

The cloud-to-cloud differences can be analyzed by both their frequency distribution and their spatial distribution, where for a better visualization of the scene and understanding trends, we divide the area into three subareas (Figure 9), grouping together territory portions with similar characteristics and expected behavior: the road slice on the west (W), the middle part full of vegetation (M), and the beach slice on the east (E).
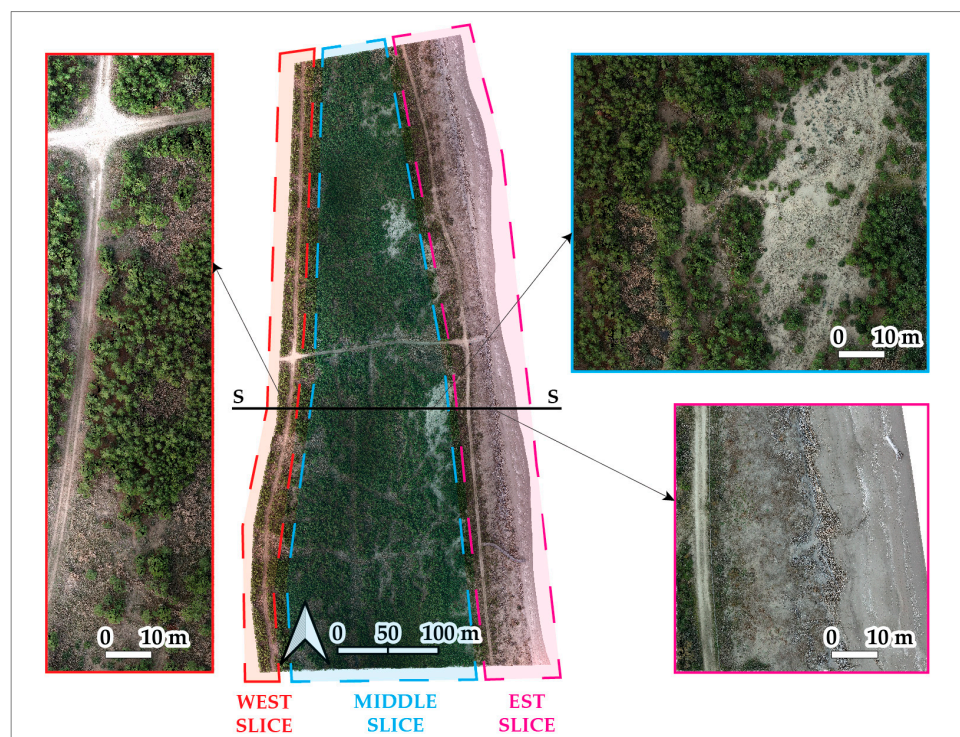

Figure 9. The subareas of interest, which group together parts of the territory with similar characteristics and behavior.

First of all, the cloud-to-cloud differences can be analyzed based on their frequency distribution, computing their statistical parameters (Table 3): all tests show a Gaussian function in a range from about -1.5 m to 2.0 m and a peak near to zero (the maximum frequent value). While the standard deviation (SD) indicates the distribution of these difference values around the mean, the root mean square (RMS) is capable of specifying the coherency between the aligned cloud and the predictive model (the reference cloud).

Table 3. Cloud-to-cloud differences after the registration procedures (reference data: registered LiDAR first echo; compared data: photogrammetric cloud). Statistics: arithmetic mean (AM); standard deviation (SD); root mean square (RMS); maximum frequent value (peak); maximum value; minimum value; percentile of the acceptability range ($|x| \leq |\pm 2\sigma_\Delta|$); and percentile of the negligibility range ($|x| \leq |\pm \sigma_\Delta|$).

	Test 0	Test α	Test β	Test γ
Arithmetic mean [cm]	3.2	-2.3	1.7	2.6
Standard deviation [cm]	7.7	8.7	7.7	7.9
Root mean square [cm]	8.3	9.0	7.9	8.3
Peak [cm]	0.5	-0.6	0.5	-0.2
Maximum [m]	2.1	1.9	2.1	2.2
Minimum [m]	-1.3	-1.5	-1.3	-1.3
Percentile $|x| \leq |\leq 2\sigma_\Delta|$ [%]	91	87	92	92
Percentile $|x| \leq |\leq \sigma_\Delta|$ [%]	72	67	74	75

When the arithmetic mean is near to zero, RMS and SD converge, indicating the lack of systematic errors. In this sense, test β, above all, shows not only a lower RMS value but also a better convergence of SD and RMS; however, it is not sufficient to represent the success of the co-registration procedure.

In fact, the presence of biases is expected using sensors that reconstruct differently the vegetation, and all tests have an arithmetic mean different from zero, i.e., a Gaussian function not symmetric around the zero value. Moreover, analyzing the arithmetic mean and percentile values, these values show that test 0, test β, and test γ have a similar trend, while test α is the only one with a compensation of the measurement on the negative part of the graph with a less percentage of points in the acceptability and negligibility range. These discrepancies suggest a different trend of test α from the others and from the validating product (test 0), where the spatial distribution of these differences can help better understand this behavior, revealing the presence of critical regions and trends.

Ideally, the expected result is to have more coherency between the clouds in the stable portions of the territory, such as the beach and the roads, and a worst coherency in the vegetated areas. However, as shown in Figure 10b, the result does not always have this type of behavior.

When the entire first echo is taken into account in the ICP procedure (test α, Figure 10b), the discrepancy between the photogrammetric vegetation reconstruction and the LiDAR vegetation reconstruction can cause a rotation of the aligned cloud, showing a decreasing coherency moving from the east slice to the west, with a subsequent rise in the height differences. The east slice exhibits a coherency within the negligibility range (-7 cm $\leq x \leq 7$ cm, gray color), while the west slice shows differences in the inaccuracy range ($x < -14$ cm, blue color), along the road path.
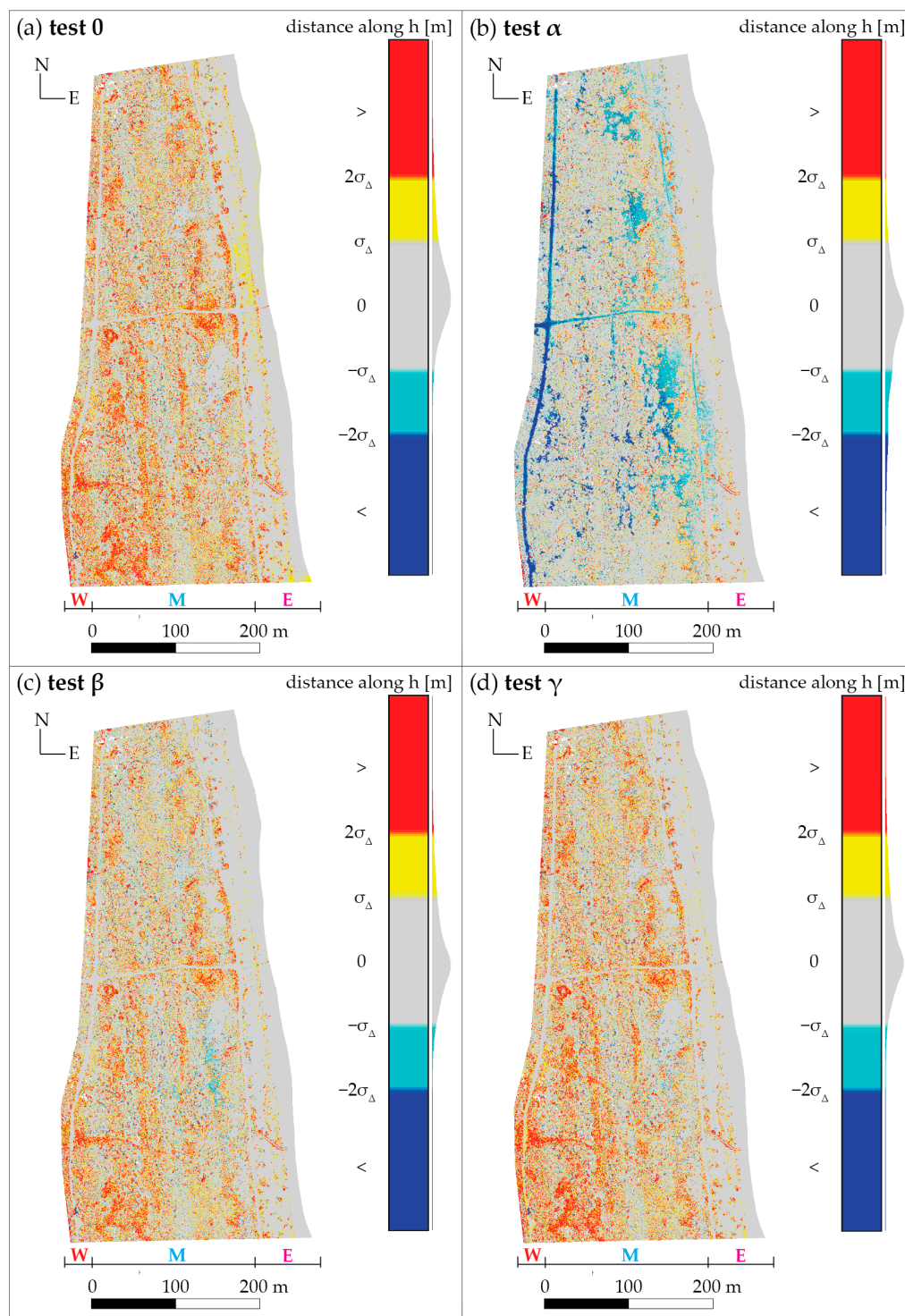
Figure 10. The cloud-to-cloud difference results using the registered LiDAR fist echo as the reference data and the photogrammetric cloud as the compared data: (**a**) test 0; (**b**) test α; (**c**) test β; and (**d**) test γ. Test α shows a decreasing coherence in the stable parts, going from the east to the west (blue color). Test 0, test β, and test γ are coherent in the stable areas (gray values) with the presence of well-spread discrepancies (red and yellow colors), linked to the dissimilarity of the vegetation reconstruction by the two sensors ($\sigma_\Delta = 7$ cm).

For this reason, in order to mitigate the bad influence of the vegetation, we conducted test β (Figure 10c) and test γ (Figure 10d), where the former uses the manual removal of the vegetation, and the latter uses the automatic ground/not ground classification. Even if there are some dissimilarities, these tests show both acceptable outcomes, because the

stable areas of the beach and the roads have values within the acceptability range and mainly in the negligibility range (gray color).

Test 0 (Figure 10a), the validating product, exhibits great coherency in the stable parts (gray values) and well-spread differences (red and yellow colors) compatible with the high and small vegetation, emphasizing the natural dissimilarity in the vegetation reconstruction by the two sensors. In this sense, test β and test γ show a similar behavior to test 0, especially for the high vegetation, with homogeneously spread differences (red and yellow colors); instead, in test α, as mentioned before, the vegetation leads to a cloud rotation and hence to differences not well spread on the territory but located in specific areas.

The extraction of section S-S (Figure 11) can help understand the different cloud trends in relation to the subarea of interest: test 0 (magenta color) shows a behavior consistent in all the slices, not linked to the nature of the clouds; test α (orange color) is coherent only in the east slice, and going from the east to the west, there is an increase in the height differences; test β and test γ (green and blue colors) show good coherency in all the slices; however, test β is more strictly connected to the east and west slices.
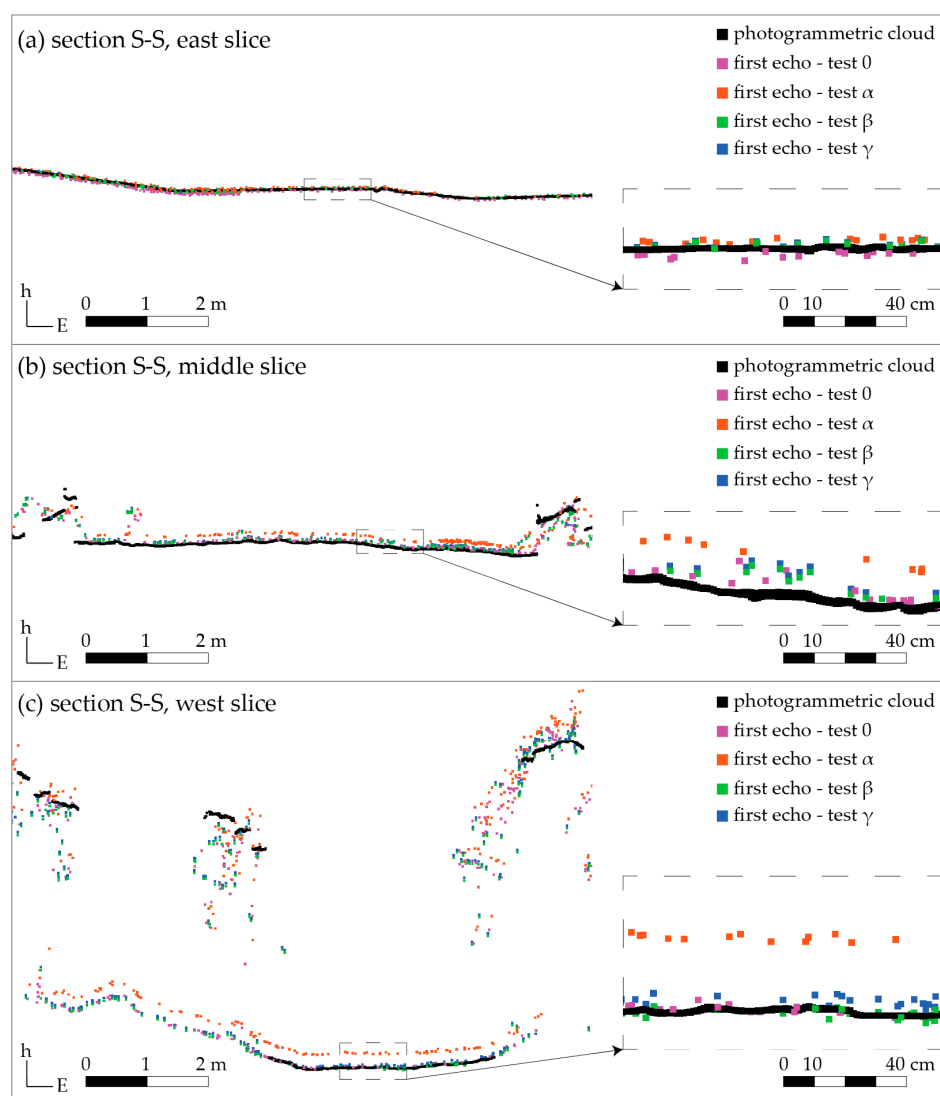

Figure 11. Section S-S: (**a**) east slice, (**b**) middle slice, and (**c**) west slice. Test 0, test β, and test γ show a good coherency in all the slices, while test α shows an increasing discrepancy going from the east to the west. The location of S-S profile is shown in Figure 9.

This divergence is compatible with the nature of the vegetation removal: test β gives weight only on the west and east slices; instead, test γ gives a uniform weight on all the territory and also in the middle part where there may be some natural differences between the photogrammetric and LiDAR reconstructions.

3.2. Target-to-Target Difference

While the cloud-to-cloud differences, described before, have assessed the co-registration results along the height component, the comparison of the coordinates between the ground points (acquired by the GNSS receiver) and the collimated one (coordinates after the registration process) gives the possibility of evaluating the co-registration differently, assessing also the east and north components.

A possible systematic error in the registration can be deduced by the non-convergence of SD and RMS, given that the SD indicates the distribution of the differences around the mean and the RMS specifies the coherence between the location of the collimated targets and the predictive targets (acquired by the GNSS receiver).

The comparison of the target coordinates (Table 4) indicates a behavior coherent with the global distribution of the differences for three reasons: (*i*) while test β and test γ have an RMS of few centimeters, test α reaches a higher value with an RMS of 14.1 cm in the height component; (*ii*) test α shows the greatest discrepancy between RMS and SD (along the height component); and (*iii*) while test α has its own trend, the outcomes of test β and test γ are compatible with test 0 (the validating product), and the maximum differences estimated for these tests (β, γ, 0) are linked to the same points (di006 for the north and di004 for the east component), emphasizing the problem of the target collimation on a coarse resolution cloud.

Table 4. The comparison of the target coordinates: the cartographic coordinates of the targets collected on the area and the corresponding collimated points on the LiDAR cloud after the registration procedures. Statistics: arithmetic mean (AM); standard deviation (SD); root mean square (RMS); maximum absolute value (max).

	AM [cm]			SD [cm]			RMS [cm]			Max [cm]		
	dN	dE	dh	dN	dE	dh	dN	dN	dN	dN	dE	dh
test 0	−0.8	−0.1	1.4	2.7	3.9	1.8	5.9	5.9	5.9	5.9	6.9	4.8
test α	−2.4	−3.4	−11.1	2.6	4.1	8.7	5.1	5.1	5.1	5.1	11.7	24.1
test β	2.4	0.2	−2	2.6	3.9	1.9	9.0	9.0	9.0	9.0	7.1	4.9
test γ	2.5	0.1	0.1	2.6	3.9	2.9	9.1	9.1	9.1	9.1	7.1	4.5

As said before, the differences between SD and RMS can be defined as systematic errors in the registration process, although, if present, they are quite small for test 0, test β, and test γ. In particular, there appears to be a bias along the height component for test 0, probably related to the major inaccuracy of the GNSS acquisition of the target coordinates along that axis; instead, while test γ has a better convergence, test β shows a similar trend to test 0, presumably related to the cloud portion used for the ICP procedure, strictly connected to the target distribution and its associated errors. Moreover, while along the east component all tests show consistent RMS and SD values, along the north component both test β and test γ exhibit a divergence, which is not present in the validating product (test 0). Having a bias along the north component, although of small magnitude (about 2.5 cm), can be expected, due to the lack of peculiarity along that axis, emphasizing a critical issue of the ICP algorithm.

4. Discussion and Conclusions

The UAV system is a cost-efficient instrument, and the application of which can be adapted to the scale of the object, the morphology of the terrain, and the requirement of the survey, allowing the collection of high-resolution data in a short period of time. A UAV system is a reliable method to monitor limited extensions of the littoral, especially since it can be exploited with different sensors (integrated or interchangeable) and can be deployed in locations that are otherwise inaccessible, eliminating the necessity for direct contact with the object.

The UAV data elaboration, and generally the reality-based modeling, is not a unique pipeline, but it can be shaped by different factors, such as the availability of data, the elaboration choices, the user's experience, and of course the final goal of the survey. In this context, the user collects and elaborates data by choosing the best pipeline possible, according to the survey needs. However, for monitoring purposes, the mere collection and reconstruction of the scene is inadequate. It is, in fact, necessary to define a unique reference system to which multiple epochs and outputs must be co-registered, facilitating the integration and comparison of the data. In this sense, the GNSS data recorded during the UAV flight combined with a positioning correction method, such as RTK, NRTK, or PPK, enable the direct georeferencing of the model. The PPK is based on a post-processing correction of the UAV position, while the RTK and NRTK are based on a real-time correction of its position, so they can easily be affected by signal loss or problems in fixing the ambiguity. The success of direct georeferencing is mainly related to the accuracy of the GNSS data and to the sensor calibration (INS, camera, etc.) onboard the UAV system, thus not providing the possibility of cross control on the effectiveness of the georeferencing procedure. Sometimes, the survey and the elaboration needs require an indirect georeferencing method in order to enhance the robustness of the computation, exploiting, for example, the knowledge of the GCP coordinates or the ICP procedure.

In this work, the survey of about 17 ha of the Adriatic littoral near the Bevano river mouth (Ravenna, Emilia-Romagna, Italy) is performed by means of a UAV system (DJI Matrice 300 RTK) with both a LiDAR sensor (L1) and an optical camera (P1) onboard, used sequentially in two different flights. The GNSS data of the flight position are computed relative to the base station (D-RTK 2), but for the model georeferencing, a network of ground points is collected by means of the GNSS receiver TopCon Hiper V with an NRTK positioning correction mode.

Of course, it is not commonly affordable to collect the same area with different sensors, but it gives the opportunity of comparing the potential and limits of each of them.

The photogrammetric technique allows the generation of a 3D reconstruction of the scene, through the elaboration of a series of overlapping images. However, the coastal environment is critical for this type of technique. First of all, the optical acquisition does not capture ground points hidden by vegetation and has a worse reconstruction of vegetated areas, and the execution of the reconstruction can be easily affected by different factors, such as moving elements, homogeneous textured areas, the nadiral pattern of acquisition, the morphology of the scene, etc.

The LiDAR data grant a better reconstruction of the vegetation and, due to the multi-echo technology, allows the collection of ground data hidden by the vegetation, making affordable the creation of a Digital Terrain Model (DTM).

In these terms, the LiDAR cloud seems to be more suitable to describe the complexity of a coastal environment, especially when a great part of vegetated areas is present in the scene. However, another relevant aspect is related to the control that the user has on the elaboration and on the result assessment.

The photogrammetric elaboration has inherent redundancy and allows an easy introduction in the computation of heterogeneous measurement (tie points, the GNSS data of the flight positions, GCP coordinates, etc.), giving to the user a higher control on the accuracy assessment of the final output, related on the residual associated with the camera position, and to the GCPs and check points used.

The LiDAR data do not have inherent redundancy, and a wrong estimation of the range data cannot be easily detected. The introduction of heterogeneous measurement into LiDAR processing is not entirely clear due to the inadequate cloud resolution, and the user has a lower control on the accuracy assessment of the result, which is mainly associated with the accuracy of the GNSS data and with the sensor calibration onboard the UAV.

In this context, the main topic of this work is to evaluate the ICP procedure used to roto-translate a LiDAR cloud (slave) into the same reference system as the photogrammetric one (master), in order to have both representations registered in the reference system RDN2008/UTM33. These two clouds represent two different descriptions of the same survey epoch.

Usually, the implementation of a network of GCPs provides assurance regarding the transformation accuracy, which is associated with the accuracy of the point acquisition and their collimation. However, it necessitates both the collection of measurements on the ground and the visibility of these points on the collected data. Typically, this does not pose a challenge for the image data, where the GCP coordinates can be integrated during the photogrammetric processing by collimating the targets on high-resolution images. For example, in this work, we reach an RMS value of 5.3 cm for the check points. In contrast, this can present an issue for the LiDAR data, due to the poor cloud resolution that renders the targets not visible or collimated with poor accuracy. For this reason, in this work, the target-based registration is not presented as a common affordable solution for registering UAV LiDAR clouds but rather as validating registration (test 0) for the ICP tests performed (test α, test β, test γ).

The results of the ICP procedure demonstrate the capability of co-registration in the absence of measurements collected on the ground, relying exclusively on the required overlapping area between the clouds. This algorithm facilitates a transformation from the reference system of the slave cloud to the master one, minimizing the distance between the two clouds. However, the lack of object distinctiveness or the presence of differences between the clouds can affect this automatic procedure, leading to improper co-registration. For example, acquiring the same object in the same temporal range by two different sensors and acquiring the same object but in different epochs are two common cases that can produce clouds with incoherency especially related to specific areas. In this work, the major problematic areas are the vegetated one, because they are reconstructed differently by the LIDAR technique and the photogrammetric elaboration.

When analyzing the cloud-to-cloud difference along the height component between the registered first echo and the photogrammetric cloud: if the ICP registration is performed without any further consideration (test α), these dissimilarities lead to a rotation of the slave cloud (LiDAR one) with an increase in the computed differences along the height component (above the acceptability range of ± 14 cm), as shown in the localized errors (blue color) along the west slice (Figure 10b); if the ICP registration is performed considering the impact of these dissimilarities (test β and test γ), the outcome can be considerably improved. In other words, the manual (test β) or automatic (test γ) removal of the cause of these dissimilarities is able to enhance the ICP solution, reaching a better coherency especially in the stable areas (roads and beach) with well-spread discrepancies mainly in the negligibility range (below 7 cm) and related to the expected differences in the reconstruction of the vegetation by the two sensors.

The analysis of the target-to-target difference (acquired by the GNSS receiver and collimated on the transformed LiDAR cloud) provides a similar trend of the cloud-to-cloud difference in the height component, also showing the presence of a small systematic error (about 2.5 cm) along the north component and it is related to the lack of beach distinctiveness along the longitudinal axis. While the critical issues related to dissimilarities between the two clouds can be reduced, the lack of object distinctiveness typical of environmental object is a significant problem that cannot be overcome with the ICP algorithm.

Moreover, as an additional consideration, the improved ICP procedures (test β and test γ) show a behavior consistent with the validating registration (target-based, test 0), while the raw ICP (test α) is the only one that shows a distinct trend, indicating the use of an improper co-registration procedure. In other words, in this specific case, characterized by a multi-sensor and single-epoch survey, the ICP algorithm can be an asset for the co-registration of the outputs, if the user is capable of firstly detecting and eliminating potential error causes, thus minimizing the need for ground measurements.

This is a specific and simpler case, because a single-epoch survey has the advantage of ensuring the presence of stable portions that can be used for a proper ICP procedure. However, environmental objects are typically surveyed for monitoring purposes, and they can be significantly impacted by natural changes, especially the coastal zones. For these reasons, considering a periodic monitoring survey in coastal areas (a multi-epoch and multi-sensor survey), the ICP procedure might not be the most suitable choice, because there is a combination of both the dissimilarities tied to the sensors used and the dissimilarities linked to the natural changes in the morphology of the territory.

This overview indicates that, under all circumstances, the user must be aware of both the potentialities and the limitations of the chosen survey technique and the corresponding registration procedure to limit, identify, and understand the occurrence of potential errors: when the georeferencing is a key point of the survey, it is important to evaluate not only how the object can be described by the chosen sensor, but also how the registration procedure can be affected by the type of data and the object characteristics, and not by neglecting the definition of a method for the evaluation of the reconstruction accuracy.

Conflicts of Interest: The authors declare no conflicts of interest.

References

1. Ciavola, P.; Armaroli, C.; Chiggiato, J.; Valentini, A.; Deserti, M.; Perini, L.; Luciani, P.; Silvani, V. Impact of Storms along the Coastline of Emilia-Romagna: The Morphological Signature on the Ravenna Coastline (Italy). *J. Coast. Res.* **2007**, *5*, 540–544. [CrossRef]
2. Sytnik, O.; Del Río, L.; Greggio, N.; Bonetti, J. Historical Shoreline Trend Analysis and Drivers of Coastal Change along the Ravenna Coast, NE Adriatic. *Environ. Earth Sci.* **2018**, *77*, 779. [CrossRef]
3. Teatini, P.; Ferronato, M.; Gambolati, G.; Bertoni, W.; Gonella, M. A Century of Land Subsidence in Ravenna, Italy. *Environ. Geol.* **2005**, *47*, 831–846. [CrossRef]
4. Calabrese, L.; Luciani, P.; Perini, L. A Review of Impact of Subsidence Induced by Gas Exploitation on Costal Erosion in Emilia-Romagna, Italy. *Boll. Geofis. Teor. Appl.* **2021**, *62*, 279–300. [CrossRef]
5. Bonaldo, D.; Antonioli, F.; Archetti, R.; Bezzi, A.; Correggiari, A.; Davolio, S.; De Falco, G.; Fantini, M.; Fontolan, G.; Furlani, S.; et al. Integrating Multidisciplinary Instruments for Assessing Coastal Vulnerability to Erosion and Sea Level Rise: Lessons and Challenges from the Adriatic Sea, Italy. *J. Coast. Conserv.* **2019**, *23*, 19–37. [CrossRef]
6. Vecchi, E.; Tavasci, L.; De Nigris, N.; Gandolfi, S. GNSS and Photogrammetric UAV Derived Data for Coastal Monitoring: A Case of Study in Emilia-Romagna, Italy. *J. Mar. Sci. Eng.* **2021**, *9*, 1194. [CrossRef]
7. Zanutta, A.; Lambertini, A.; Vittuari, L. UAV Photogrammetry and Ground Surveys as a Mapping Tool for Quickly Monitoring Shoreline and Beach Changes. *J. Mar. Sci. Eng.* **2020**, *8*, 52. [CrossRef]
8. Duo, E.; Trembanis, A.C.; Dohner, S.; Grottoli, E.; Ciavola, P. Local-Scale Post-Event Assessments with GPS and UAV-Based Quick-Response Surveys: A Pilot Case from the Emilia–Romagna (Italy) Coast. *Nat. Hazards Earth Syst. Sci.* **2018**, *18*, 2969–2989. [CrossRef]
9. Holman, R.A.; Stanley, J. The History and Technical Capabilities of Argus. *Coast. Eng.* **2007**, *54*, 477–491. [CrossRef]
10. Addona, F.; Sistilli, F.; Romagnoli, C.; Cantelli, L.; Liserra, T.; Archetti, R. Use of a Raspberry-Pi Video Camera for Coastal Flooding Vulnerability Assessment: The Case of Riccione (Italy). *Water* **2022**, *14*, 999. [CrossRef]
11. Guariglia, A.; Buonamassa, A.; Losurdo, A.; Saladino, R.; Trivigno, M.; Zaccagnino, A.; Colangelo, A. A Multisource Approach for Coastline Mapping and Identification of Shoreline Changes. *Ann. Geophys.* **2009**, *49*, 205–304. [CrossRef]
12. Alesheikh, A.A.; Ghorbanali, A.; Nouri, N. Coastline Change Detection Using Remote Sensing. *Int. J. Environ. Sci. Technol.* **2007**, *4*, 61–66. [CrossRef]
13. Alicandro, M.; Baiocchi, V.; Brigante, R.; Radicioni, F. Automatic Shoreline Detection from Eight-Band VHR Satellite Imagery. *J. Mar. Sci. Eng.* **2019**, *7*, 459. [CrossRef]
14. Tajima, Y.; Wu, L.; Watanabe, K. Development of a Shoreline Detection Method Using an Artificial Neural Network Based on Satellite SAR Imagery. *Remote Sens.* **2021**, *13*, 2254. [CrossRef]
15. Stockdonf, H.F.; Sallenger, A.H., Jr.; List, J.H.; Holman, R.A. Estimation of Shoreline Position and Change Using Airborne Topographic Lidar Data. *J. Coast. Res.* **2002**, *18*, 502–513.
16. Le Mauff, B.; Juigner, M.; Ba, A.; Robin, M.; Launeau, P.; Fattal, P. Coastal Monitoring Solutions of the Geomorphological Response of Beach-Dune Systems Using Multi-Temporal LiDAR Datasets (Vendée Coast, France). *Geomorphology* **2018**, *304*, 121–140. [CrossRef]
17. Gonçalves, J.A.; Henriques, R. UAV Photogrammetry for Topographic Monitoring of Coastal Areas. *ISPRS J. Photogramm. Remote Sens.* **2015**, *104*, 101–111. [CrossRef]
18. Faelga, R.A.; Cantelli, L.; Silvestri, S.; Giambastiani, B.M.S. Dune Belt Restoration Effectiveness Assessed by UAV Topographic Surveys (Northern Adriatic Coast, Italy). *Biogeosciences* **2023**, *20*, 4841–4855. [CrossRef]
19. Turner, I.L.; Harley, M.D.; Drummond, C.D. UAVs for Coastal Surveying. *Coast. Eng.* **2016**, *114*, 19–24. [CrossRef]
20. Espriella, M.C.; Lecours, V. Optimizing the Scale of Observation for Intertidal Habitat Classification through Multiscale Analysis. *Drones* **2022**, *6*, 140. [CrossRef]
21. Tools and Acquisition Protocols for Enhancing Artifacts Documentation (TAPENADE). Available online: http://www.tapenade.gamsau.archi.fr/TAPEnADe/Protocols.html (accessed on 25 October 2024).
22. Türk, T.; Tunalioglu, N.; Erdogan, B.; Ocalan, T.; Gurturk, M. Accuracy Assessment of UAV-Post-Processing Kinematic (PPK) and UAV-Traditional (with Ground Control Points) Georeferencing Methods. *Environ. Monit. Assess.* **2022**, *194*, 476. [CrossRef]
23. Czyża, S.; Szuniewicz, K.; Kowalczyk, K.; Dumalski, A.; Ogrodniczak, M.; Zieleniewicz, Ł. Assessment of Accuracy in Unmanned Aerial Vehicle (UAV) Pose Estimation with the REAL-Time Kinematic (RTK) Method on the Example of DJI Matrice 300 RTK. *Sensors* **2023**, *23*, 2092. [CrossRef]
24. Bolkas, D. Assessment of GCP Number and Separation Distance for Small UAS Surveys with and without GNSS-PPK Positioning. *J. Surv. Eng.* **2019**, *145*, 04019007. [CrossRef]

25. Tournadre, V.; Pierrot-Deseilligny, M.; Faure, P.H. UAV LINEAR PHOTOGRAMMETRY. *Int. Arch. Photogramm. Remote Sens. Spat. Inf. Sci.* **2015**, *XL-3-W3*, 327–333. [CrossRef]

26. Ramos, M.M.; Remondino, F. Data Fusion in Cultural Heritage—A Review. *Int. Arch. Photogramm. Remote Sens. Spat. Inf. Sci.* **2015**, *XL-5-W7*, 359–363. [CrossRef]

27. Triggs, B.; McLauchlan, P.F.; Hartley, R.I.; Fitzgibbon, A.W. Bundle Adjustment—A Modern Synthesis. In *Vision Algorithms: Theory and Practice*; Triggs, B., Zisserman, A., Szeliski, R., Eds.; Springer: Berlin/Heidelberg, Germany, 2000; pp. 298–372.

28. Agarwal, S.; Snavely, N.; Simon, I.; Seitz, S.M.; Szeliski, R. Building Rome in a Day. In Proceedings of the 2009 IEEE 12th International Conference on Computer Vision, Kyoto, Japan, 29 September–2 October 2009; pp. 72–79.

29. Schenk, T.; Department, C.; Csatho, B. Fusion of LIDAR Data and Aerial Imagery for a More Complete Surface Description. *Int. Arch. Photogramm. Remote Sens. Spat. Inf. Sci.* **2002**, *XXXIV Part. 3 A+B*, 310–317.

30. Vosselman, G.; Maas, H.-G. *Airborne and Terrestrial Laser Scanning*; Whittles Publishing: Dunbeath, UK, 2010; ISBN 978-1-904445-87-6.

31. Xu, N.; Qin, R.; Song, S. Point Cloud Registration for LiDAR and Photogrammetric Data: A Critical Synthesis and Performance Analysis on Classic and Deep Learning Algorithms. *ISPRS Open J. Photogramm. Remote Sens.* **2023**, *8*, 100032. [CrossRef]

32. Rabbani, T.; Dijkman, S.; van den Heuvel, F.; Vosselman, G. An Integrated Approach for Modelling and Global Registration of Point Clouds. *ISPRS J. Photogramm. Remote Sens.* **2007**, *61*, 355–370. [CrossRef]

33. Habib, A.; Ghanma, M.; Morgan, M.; Al-Ruzouq, R. Photogrammetric and Lidar Data Registration Using Linear Features. *Photogramm. Eng. Remote Sens.* **2005**, *71*, 699–707. [CrossRef]

34. Gruen, A.; Akca, D. Least Squares 3D Surface and Curve Matching. *ISPRS J. Photogramm. Remote Sens.* **2005**, *59*, 151–174. [CrossRef]

35. Besl, P.J.; McKay, N.D. A Method for Registration of 3-D Shapes. *IEEE Trans. Pattern Anal. Mach. Intell.* **1992**, *14*, 239–256. [CrossRef]

36. Myronenko, A.; Song, X. Point Set Registration: Coherent Point Drift. *IEEE Trans. Pattern Anal. Mach. Intell.* **2010**, *32*, 2262–2275. [CrossRef] [PubMed]

37. Martínez-Carricondo, P.; Carvajal-Ramírez, F.; Agüera-Vega, F. Co-Registration of Multi-Sensor UAV Imagery. Case Study: Boreal Forest Areas. *Scand. J. For. Res.* **2022**, *37*, 227–240. [CrossRef]

38. Aicardi, I.; Nex, F.; Gerke, M.; Lingua, A.M. An Image-Based Approach for the Co-Registration of Multi-Temporal UAV Image Datasets. *Remote Sens.* **2016**, *8*, 779. [CrossRef]

39. Shao, J.; Yao, W.; Wan, P.; Luo, L.; Wang, P.; Yang, L.; Lyu, J.; Zhang, W. Efficient Co-Registration of UAV and Ground LiDAR Forest Point Clouds Based on Canopy Shapes. *Int. J. Appl. Earth Obs. Geoinf.* **2022**, *114*, 103067. [CrossRef]

40. Persad, R.A.; Armenakis, C. Automatic Co-Registration of 3D Multi-Sensor Point Clouds. *ISPRS J. Photogramm. Remote Sens.* **2017**, *130*, 162–186. [CrossRef]

41. Zhao, H.; Li, G.; Chen, Z.; Zhang, S.; Zhang, B.; Cheng, X. Impacts of GCP Distributions on UAV-PPK Photogrammetry at Sermeq Avannarleq Glacier, Greenland. *Remote Sens.* **2024**, *16*, 3934. [CrossRef]

42. Pilartes-Congo, J.A.; Simpson, C.; Starek, M.J.; Berryhill, J.; Parrish, C.E.; Slocum, R.K. Empirical Evaluation and Simulation of the Impact of Global Navigation Satellite System Solutions on Uncrewed Aircraft System–Structure from Motion for Shoreline Mapping and Charting. *Drones* **2024**, *8*, 646. [CrossRef]

43. Shaw, L.; Helmholz, P.; Belton, D.; Addy, N. COMPARISON OF UAV LIDAR AND IMAGERY FOR BEACH MONITORING. *Int. Arch. Photogramm. Remote Sens. Spat. Inf. Sci.* **2019**, *XLII-2-W13*, 589–596. [CrossRef]

44. LIFE NatuReef. Available online: https://site.unibo.it/life-natureef (accessed on 12 June 2024).

45. NETGEO. Available online: http://www.netgeo.it/page.php?Id=62 (accessed on 21 October 2024).

46. Wanninger, L. Virtual Reference Stations (VRS). *GPS Solut.* **2003**, *7*, 143–144. [CrossRef]

47. Farolfi, G.; Maseroli, R.; Baroni, L.; Cauli, F. Final Results of the Italian «Rete Dinamica Nazionale» (RDN) of Istituto Geografico Militare Italiano (IGMI) and Its Alignment to ETRF2000. *Boll. Geod. Sci. Affin.* **2009**, *3*, 287–320.

48. Giorgini, E.; Vecchi, E.; Poluzzi, L.; Tavasci, L.; Barbarella, M.; Gandolfi, S. 15 Years of the Italian GNSS Geodetic Reference Frame (RDN): Preliminary Analysis and Considerations. In *Geomatics for Green and Digital Transition*; Borgogno-Mondino, E., Zamperlin, P., Eds.; Springer International Publishing: Cham, Switzerland, 2022; pp. 3–14.

49. Cai, Y.; Cheng, P.; Meng, X.; Tang, W.; Shi, C. Using Network RTK Corrections and Low-Cost GPS Receiver for Precise Mass Market Positioning and Navigation Applications. In Proceedings of the 2011 IEEE Intelligent Vehicles Symposium (IV), Baden-Baden, Germany, 5–9 June 2011; pp. 345–349.

50. Gumus, K. Studying the Repeatability of Measurements Obtained via Network Real-Time Kinematic Positioning at Different Times of the Day. *Ing. Investig.* **2024**, *44*, e105622. [CrossRef]

51. Dardanelli, G.; Maltese, A.; Pipitone, C.; Pisciotta, A.; Lo Brutto, M. NRTK, PPP or Static, That Is the Question. Testing Different Positioning Solutions for GNSS Survey. *Remote Sens.* **2021**, *13*, 1406. [CrossRef]

52. ConvER 2021. Available online: https://geoportale.regione.emilia-romagna.it/download/utility-e-tool/conver-2021-software (accessed on 13 September 2024).

53. Barzaghi, R.; Borghi, A.; Carrion, D.; Sona, G. Refining the Estimate of the Italian Quasi-Geoid. *Boll. Geod. Sci. Affin.* **2007**, *3*, 145–160.

54. MicMac, (v1.1.1). Available online: https://github.com/micmacIGN/micmac/releases (accessed on 21 October 2024).

55. Pierrot Deseilligny, M.; Clery, I. APERO, an Open Source Bundle Adjusment Software for Automatic Calibration and Orientation of Set of Images. *Int. Arch. Photogramm. Remote Sens. Spat. Inf. Sci.* **2012**, *XXXVIII-5-W16*, 269–276. [CrossRef]

56. Pierrot-Deseilligny, M. MicMac, Apero, Pastis and Other Beverages in a Nutshell! Available online: https://github.com/micmacIGN/Documentation/blob/master/DocMicMac.pdf (accessed on 2 January 2025).

57. Rupnik, E.; Daakir, M.; Pierrot Deseilligny, M. MicMac—A Free, Open-Source Solution for Photogrammetry. *Open Geospat. Data Softw. Stand.* **2017**, *2*, 14. [CrossRef]

58. Pierrot-Deseilligny, M.; Paparoditis, N. A Multiresolution and Optimization-Based Image Matching Approach: An Application to Surface Reconstruction from SPOT5-HRS Stereo Imagery. *Arch. Photogramm. Remote Sens. Spat. Inf. Sci.* **2006**, *XXXVI-1/W41*, 1–5.

59. Harvey, P. ExifTool, (V12.73). Available online: https://exiftool.org/ (accessed on 21 October 2024).

60. Lisein, J.; Pierrot-Deseilligny, M.; Bonnet, S.; Lejeune, P. A Photogrammetric Workflow for the Creation of a Forest Canopy Height Model from Small Unmanned Aerial System Imagery. *Forests* **2013**, *4*, 922–944. [CrossRef]

61. DJI Terra Pro, (v3.9.4). Available online: https://enterprise.dji.com/it/dji-terra (accessed on 3 September 2024).

62. CloudCompare, (v2.13.1). Available online: https://www.danielgm.net/cc/ (accessed on 3 September 2024).